


## Article

# Microstructure and Photoluminescence of $\text{ZrTiO}_4\text{:Eu}^{3+}$ Phosphors: Host-Sensitized Energy Transfer and Optical Thermometry

Anheng Gu <sup>1,2</sup>, Guo-Hui Pan <sup>1,2,\*</sup> , Huajun Wu <sup>1,2</sup>, Liangliang Zhang <sup>1,2</sup>, Ligong Zhang <sup>1</sup>, Hao Wu <sup>1,2</sup> and Jiahua Zhang <sup>1,2,\*</sup>

<sup>1</sup> State Key Laboratory of Luminescence and Applications, Changchun Institute of Optics, Fine Mechanics and Physics, Chinese Academy of Sciences, 3888 Dong Nanhu Road, Changchun 130033, China

<sup>2</sup> Center of Materials Science and Optoelectronics Engineering, University of Chinese Academy of Sciences, Beijing 100049, China

\* Correspondence: guohui.pan@aliyun.com (G.-H.P.); zhangjh@ciomp.ac.cn (J.Z.)

**Abstract:** Orthorhombic  $\text{ZrTiO}_4$  is an attractive dielectric material; its optical properties are, however, less known. In this paper, we reported on the microstructure and luminescence studies of pristine  $\text{ZrTiO}_4$  and  $\text{Eu}^{3+}$ -doped  $\text{ZrTiO}_4$  phosphors. The results indicated that two types of  $\text{TiO}_6$  octahedra, the isolated/ localized and coupled/delocalized, coexisted in host matrix.  $\text{Eu}^{3+}$  doping could induce oxygen vacancy defect states located below the bottom of the conduction band. Pristine  $\text{ZrTiO}_4$  showed bright yellow luminescence via STEs recombination at defects sites at low temperatures, but significant thermal quenching occurred due to STEs migration to quenching centers at elevated temperatures. Effective host sensitized energy transfer to  $\text{Eu}^{3+}$  was observed in  $\text{ZrTiO}_4\text{:Eu}^{3+}$  phosphors and yielded the red characteristic emissions of  $\text{Eu}^{3+}$ . Anomalous STEs luminescence enhancement and spectral blue-shift in the excitation spectra with higher  $\text{Eu}^{3+}$  concentration appeared and were explained by considering three factors: competitive absorption between electron transitions from the top of the valence band to the defect states and host conduction band,  $\text{Eu}^{3+}$  doping driving the production of more isolated  $\text{TiO}_6$  octahedra, and energy back-transfer from  $\text{Eu}^{3+}$  activators to other titanate groups. On the basis of the dual-emitting combination strategy involving host STEs and  $\text{Eu}^{3+}$  luminescence,  $\text{ZrTiO}_4\text{:Eu}^{3+}$  phosphors were demonstrated to be ratiometric self-referencing optical thermometric materials, with a working range of 153–313 K and a maxima of relative sensitivity to  $\sim 1.1\% \text{ K}^{-1}$  at 243 K.

**Keywords:** zirconium titanate; delocalization; self-trapped excitons; host-sensitized energy transfer; optical thermometry



**Citation:** Gu, A.; Pan, G.-H.; Wu, H.; Zhang, L.; Zhang, L.; Wu, H.; Zhang, J. Microstructure and Photoluminescence of  $\text{ZrTiO}_4\text{:Eu}^{3+}$  Phosphors: Host-Sensitized Energy Transfer and Optical Thermometry. *Chemosensors* **2022**, *10*, 527. <https://doi.org/10.3390/chemosensors10120527>

Academic Editor: Ilaria Rea

Received: 19 October 2022

Accepted: 16 November 2022

Published: 12 December 2022

**Publisher's Note:** MDPI stays neutral with regard to jurisdictional claims in published maps and institutional affiliations.



**Copyright:** © 2022 by the authors. Licensee MDPI, Basel, Switzerland. This article is an open access article distributed under the terms and conditions of the Creative Commons Attribution (CC BY) license (<https://creativecommons.org/licenses/by/4.0/>).

## 1. Introduction

Solid state luminescent materials or phosphors have a wide range of applications in laser, display, lighting, detection, and sensing technologies [1–5]. Such materials are typically comprised of a host that is doped with a small quantity of activators or dopants (typically including transition metal (TM) ions and lanthanide ions). For inorganic crystalline materials, the host lattice could provide a certain crystallographic symmetry of the surroundings for the activators and then modulate their luminescence properties. Achieving new types of phosphors and finding potential applications for them remains a challenge and is of great scientific and technical significance. In this connection, the searching for a novel host and the following effective doping are both essential.

Bulk zirconium titanate ( $\text{ZrTiO}_4$ ), one ternary compound in the  $\text{ZrO}_2\text{--TiO}_2$  system, is of technological importance in microwave telecommunications (as a capacitor, dielectric resonator in filters, and oscillator), memory devices (ReRAM), humidity/gas sensors, and

structural ceramic due to its high dielectric constant at microwave frequencies, high corrosion resistance, and excellent thermal stability [6–9]. Great interest has been generated in studying its microstructure, phase transformation, thermal expansivity, and dielectricity [9–13]. However, in terms of its use as a luminescent material or particularly as a host of accommodating activators, only minimal research has been conducted to date. A weak blue-white broadband photoluminescence was observed on the nanocrystalline products of ZrTiO<sub>4</sub> after heating treatment of its chemical precursor (dry-gel), but no photoluminescence was elucidated in the crystalline phase [14,15]. In this paper, we reported on the optical properties of ZrTiO<sub>4</sub> powders prepared by the solid-state reaction method, including the self-activated and doping-induced photoluminescence upon hosting trivalent lanthanide (Ln<sup>3+</sup>) ions of Eu<sup>3+</sup>. It was found that the pristine ZrTiO<sub>4</sub> shows bright yellow host luminescence at a low temperature due to the recombination of self-trapped excitons (STEs) at defect sites. Efficient host-mediated resonance energy transfer (Förster type) from STEs to Eu<sup>3+</sup> was observed upon further substitution of Eu<sup>3+</sup>, yielding the characteristic red luminescence. STEs luminescence and STEs-mediated energy transfer to Ln<sup>3+</sup> were investigated extensively in lanthanide-doped vanadates, tungstates, borates, and niobates [16–19]. It is interesting that in these crystals, the STEs were usually identified with a localized excitation of the oxy-anionic complexes (for instance, VO<sub>4</sub><sup>3-</sup>, BO<sub>3</sub><sup>3-</sup>) [17–19]. Herein, the emission of STEs was considered to be located in the TiO<sub>6</sub><sup>8-</sup> complexes but with a large amount of delocalization, which is in accordance with previous reports on other titanates (SrTiO<sub>3</sub>, BaTiO<sub>3</sub>, La<sub>2</sub>TiO<sub>5</sub>) [19–21].

Temperature is one of the fundamental thermodynamic properties and an important parameter in industry and science communities [22]. Applying luminescent materials to temperature sensing (i.e., optical thermometry) has been the subject of world-wide interest due to their fast response and noninvasive features as well as their potential in harsh environments in comparison to traditional techniques derived from variations in thermal expansion, electrical resistance, capacitance, and thermoelectricity [2–5,23,24]. Based on the temperature-dependent optical spectroscopic characteristics of phosphors, including fluorescence intensity or intensity ratio (FIR), bandwidth, band shape, polarization, spectral shift and lifetime, and many others, a variety of luminescent sensing materials have been developed in recent years [2–5,25–27]. Of particular interest is the FIR technique, a ratiometric luminescence thermometry involving the intensity of two luminescence bands, which is fundamentally more resistant to the external undulations (e.g., pumping power, sample size) than those based on the single band intensity, peak position, and the bandwidth, thus being capable of probing the temperature more accurately [2,22]. Obviously, high performance FIR based optical thermometry relies on two temperature-sensitivity-distinct luminescent bands, which could originate from one and the same luminescent centers or respectively from two different centers. The luminescence from TM ions (e.g., V<sup>5+,4+,3+</sup>, Ti<sup>3+,4+</sup>, Cr<sup>3+,4+</sup>, Mn<sup>2+,3+,4+</sup>, Fe<sup>3+</sup>, Cu<sup>2+</sup> with higher and larger activation energies) via d-d crystal-field transitions or TM(d<sup>0</sup>)→O<sup>2-</sup> charge transfer (CT) transitions is characterized by strong absorption and emission bands, and is highly susceptible to temperature variations in many cases due to bare d-orbitals and strong electron-lattice coupling [2]. They have been widely used in luminescence thermometry. In contrast, Ln<sup>3+</sup> (e.g., Eu<sup>3+</sup>, Er<sup>3+</sup>, Nd<sup>3+</sup> and Dy<sup>3+</sup>) could show more temperature-inert narrow emissions, via 4f-4f intra-configurational electronic transitions, due to the weak electron-phonon coupling as result of the good shielding of a partly-filled 4f<sup>n</sup> shell by the outer 5s and 5p orbitals [2,22]. In addition, narrow emission band/peaks could facilitate spectral separation of bands during spectral measurements [2]. It is thus expected that the combination of the luminescence of TM and Ln<sup>3+</sup> ions in one material is particularly well-suited for luminescence thermometry, and could even yield highly sensitive FIR-based optical thermometry by using Ln<sup>3+</sup> luminescence as a self-referencing standard. An overview of the state of the art of advance was reviewed recently by L. Marciniak [2]. In particular, this was exemplified by LaGaO<sub>3</sub>:V<sup>5+,4+,3+</sup>, Nd<sup>3+</sup>, and YVO<sub>4</sub>:Er<sup>3+</sup> phosphors, where the temperature-sensitive broad band luminescence of CT transition (V<sup>5+</sup>→O<sup>2-</sup>), and d-d transitions of <sup>2</sup>E→<sup>2</sup>T<sub>2</sub> (V<sup>4+</sup>), and

${}^3T_{1g} \rightarrow {}^3T_{1g}$  ( $V^{3+}$ ) were utilized as temperature indicators, while the line-like emissions of  ${}^4F_{3/2} \rightarrow {}^4I_{9/2}$  transitions of  $Nd^{3+}$  or  ${}^2H_{11/2}/{}^4S_{3/2} \rightarrow {}^4I_{15/2}$  transitions of  $Er^{3+}$  were utilized as luminescent references [28,29]; other examples included  $Cr^{3+}$ ,  $Nd^{3+}$  co-doped  $LiLaP_4O_{12}$ ,  $Cr^{3+}$ ,  $Ln^{3+}$  ( $Ln^{3+} = Nd^{3+}, Dy^{3+}, Eu^{3+}$ ) co-doped garnet phosphors ( $Gd_3Ga_5O_{12}$ ,  $Y_3Al_5O_{12}$ ). Likewise, the broad band emissions of d-d transitions of  ${}^4T_2 \rightarrow {}^4A_2$  of  $Cr^{3+}$  served as temperature signals, the corresponding internal reference signals were from  $Ln^{3+}$  ( $Nd^{3+}$ ,  ${}^4F_{3/2} \rightarrow {}^4I_{11/2}$ ;  $Dy^{3+}$ ,  ${}^4F_{9/2} \rightarrow {}^6H_{9/2,11/2,13/2}$ ;  $Eu^{3+}$ ,  ${}^5D_0 \rightarrow {}^7F_1$ ) [30–32]. A high relative sensitivity of  $S_r = 4.89\%/K$  at 323 K and sensitivities  $S_r > 15\%/K$  for temperatures in the 423–473 K range was achieved in  $LiLaP_4O_{12}: Cr^{3+}, Nd^{3+}$  due to the efficient thermal quenching of the broad band luminescence of  $Cr^{3+}$  [32]. It is worth noting that in many cases the two luminescent bands for the FIR were obtained upon single wavelength excitation into the TM ions followed by energy transfer to  $Ln^{3+}$ .

The TMs of titanium (Ti), with two oxide states of  $Ti^{3+}$  ( $3d^1$ ) and  $Ti^{4+}$  ( $3d^0$ ), were considerably less-used in luminescence thermometry, and there only exist a few reports on this when examining the literature. An earlier study in 2007 was presented by Katsumata et al. [33] on the luminescence of  $Ti^{3+}$  ions in sapphire ( $Al_2O_3$ ) crystal; they found a sublinear dependence of luminescence intensity against temperature and further demonstrated them as luminescent temperature sensors on the basis of a single emission band of crystal field transition  ${}^2E_g \rightarrow {}^2T_{2g}$  of  $Ti^{3+}$ . Recently, there has been increasing interest in exploiting Ti ions-doped powder materials toward optical thermometry, and especially in developing the FIR-based thermometry by combining  $Ti^{3+/4+}$  ions with the luminescent centers of  $Ln^{3+}$ . Examples are  $Y_3Al_5O_{12}:Ti^{4+}, Ln^{3+}$  ( $Ln^{3+} = Nd^{3+}, Eu^{3+}, Dy^{3+}$ ) by Drabik et al. [34],  $LiTaO_3:Ti^{4+}, Eu^{3+}$  by Wang et al. [35], and  $ZrO_2:Ti^{4+}, Eu^{3+}$  by us [22]. Note that in these studies, Ti plays a role of the impurity ions (dopant) at low concentrations rather than that of the host constituent. In contrast, a host of titanate (100% concentration of  $Ti^{4+}$ ) of  $Gd_2Ti_2O_7$  was developed by M. D. Dramićanin et al. [36] for luminescence thermometry upon introducing  $Eu^{3+}$  into the lattice, where the temperature indicator of the host luminescence was considered to be the trap emission induced by the oxygen vacancies—a lower relative sensitivity of  $S_r = 0.46\%K^{-1}$  at 423 K was obtained. In this study, we demonstrated the new type of titanate phosphors of  $Eu^{3+}$ -doped  $ZrTiO_4$  as FIR optical thermometry by combining the temperature-sensitive STEs broad emissions ( $Ti^{4+} \rightarrow O^{2-}$  CT type) of the host lattice and somewhat temperature-inert sharp emissions of the  $Eu^{3+}$  activator. The temperature sensing was achieved upon excitation at the absorption edge followed by host-sensitized energy transfer to  $Eu^{3+}$ , and covered a working range of 153–313 K with a maximum relative sensitivity of  $\sim 1.1\%K^{-1}$ .

## 2. Experimental

### 2.1. Chemicals and Materials Preparation

All chemicals used in this study were of analytical grade and were used without further purification. High purity starting oxides  $ZrO_2$  (99.99%, metals basis, without Hf or  $HfO_2$ ),  $TiO_2$  (99.8%, anatase, metals basis), and  $Eu_2O_3$  (99.999%) were supplied by Aladdin Industrial Inc., China. The samples of  $Zr_{1-x}Eu_xTiO_4$  ( $x = 0, 0.0001, 0.0002, 0.0005, 0.001, 0.002, 0.005, 0.01, 0.05$ ) were prepared by the high-temperature solid phase method. The starting materials according to the stoichiometric proportion were weighed, mixed, and were then ball-milled for 12 h by using a high-energy ball milling machine (Fritsch pulverisette 4, Germany) with  $ZrO_2$  grinding balls and methyl alcohol as the dispersant. The resulting slurry was then dried in an oven at 60 °C in air, followed by calcining in a high-temperature muffle furnace at 1300 °C for 4 h in air.

### 2.2. Characterization and Measurements

The phase purity and crystalline structure were checked by X-ray power diffraction (XRD) techniques on a powder diffractometer (D8 Advance, Bruker, Billerica, MA, USA), which was operated at 40 kV and 30 mA in the range from 20° to 65° with  $Cu-K\alpha$  radiation. The morphology and energy dispersive X-ray spectroscopy (EDS) were characterized by

scanning electron microscopy (SEM, S-4800, Hitachi, Tokyo, Japan). The diffuse reflectance (DR) spectra in the 200–800 nm region were recorded by using a dual beam UV-vis-NIR spectrophotometer (UV-3600 plus, Shimadzu, Kyoto, Japan) equipped with an integrating sphere assembly (150 nm), with BaSO<sub>4</sub> as a reference standard. Raman spectra were acquired on an Infinity Raman spectrometer (Horiba Jobin Yvon, Paris, France) with a 488 nm laser excitation source (He-Cd laser, Wavicle, Beijing, China). Steady state photoluminescence (PL) spectra were recorded on a FLS 920 spectrofluorometer (Edinburgh Instruments, Edinburgh, UK) with a 450 W xenon lamp as the excitation source. The emission spectra were corrected to the instrument responses. The fluorescence decays in the microsecond and millisecond scales were conducted by using an optical parametric oscillator (OPO) as the pulse excitation source, and the signals were analyzed by using a spectrometer (Triax550, Horiba, Paris, France) and a digital oscilloscope (TDS3052, Tektronix, Beaverton, OR, USA), while those in the nanosecond scale were obtained by using the time-correlated single-photon counting method on a spectrofluorometer (FLS 920, Edinburgh Instruments, UK) equipped with a photon counting detector of photomultiplier tube (PMT) R928 and a hydrogen flash lamp as the excitation source. For temperature-dependent (153–313 K) PL measurements, the powdered samples were placed on a heating and cooling stage (THMS-600, Linkam, Salfords, UK) mounted on the objective table of an upright fluorescence microscope (BX53M, Olympus, Tokyo, Japan) jointed sideways with a fiber optic spectrometer (QEPro, Ocean Optics, Largo, FL, USA). An excitation irradiation in the range of 340–370 nm from a mercury burner lamp (130 W) was selected by a band-pass filter. Fluorescence signals were collected with an objective lens and focused onto the entrance of the distal end of the combined fiber of the spectrometer. Both illuminations of the surface and detection of the fluorescence were performed along an axis coincident with the surface normal. A cooled digital color camera (DP74, Olympus, Tokyo, Japan) equipped on the microscope was used for fluorescence microscopy and photograph capture. All the measurements were carried out at room temperature unless otherwise noted.

### 3. Results and Discussion

#### 3.1. Composition, Crystalline Structure and Morphology

Zirconium titanate may exist in a number of modifications in the ZrO<sub>2</sub>–TiO<sub>2</sub> phase diagram. Zirconium orthotitanate of ZrTiO<sub>4</sub>, with equivalent amounts of Ti<sup>4+</sup> and Zr<sup>4+</sup> ions in the composition, is one of the stable ternary compounds [11]. It has the orthorhombic  $\alpha$ -PbO<sub>2</sub>-type structure with *Pbcn* space group, where Ti<sup>4+</sup> and Zr<sup>4+</sup> ions are both randomly distributed on an octahedral site of 4c2 (Wyckoff notation)—which are quite disordered [7,11]. This structure is extremely similar to those of TiO<sub>2</sub> polymorphs consisting of edge-shearing TiO<sub>6</sub> octahedra [7,13]. The phase purity of Zr<sub>1-x</sub>Eu<sub>x</sub>TiO<sub>4</sub> powders under investigation was checked by XRD analysis, as was shown in Figure 1a together with the diffraction lines of a reference ZrTiO<sub>4</sub> (PDF#74-1504). It was found that at the lower doping concentration ( $x \leq 0.01$ ) of Eu<sup>3+</sup>, all the peaks of the diffraction pattern of the samples correspond the ZrTiO<sub>4</sub> phase. No evidence of the presence of any peaks of impurities was observed. A small quantity of impurities, however, appeared in the samples at higher doping concentration, as was indicated by asterisks in the figure for a typical sample of Zr<sub>1-x</sub>Eu<sub>x</sub>TiO<sub>4</sub> ( $x = 0.05$ ). This was tentatively assigned to the Zr<sub>5</sub>Ti<sub>7</sub>O<sub>24</sub> phase. Semi-quantitative EDS analysis (see Figure S1) confirmed the presence of Eu<sup>3+</sup> in the sample when its doping concentration was higher ( $x = 0.05$ ). The presence of such impurities was thus attributed to the aliovalent substitution, where the trivalent Eu<sup>3+</sup> located on a site normally occupied by a tetravalent host ion of Zr<sup>4+</sup>, leaving an effective negative charge at that site and creating 0.5 positively charged extrinsic oxygen vacancy for charge compensation. The incorporation reaction can be expressed as:



where an oxygen vacancy can compensate two  $\text{Eu}^{3+}$  ions either locally or distantly. It was considered that a larger mismatch of ionic radius of between  $\text{Eu}^{3+}$  (0.95 Å, CN = 6) and  $\text{Zr}^{4+}$  (0.72 Å, CN = 6) and a higher concentration of oxygen vacancy induced by the incorporation of more  $\text{Eu}^{3+}$  caused the great distortion of lattices and then the occurrence of phase change. Additionally, when increasing the doping level ( $x$ ) of  $\text{Eu}^{3+}$  ions, the (111) diffraction peaks gradually shift toward larger  $2\theta$  angles (the right part of Figure 1a), suggesting a contraction of the lattice cell upon  $\text{Eu}^{3+}$  substitution due to the presence of oxygen vacancy defects.

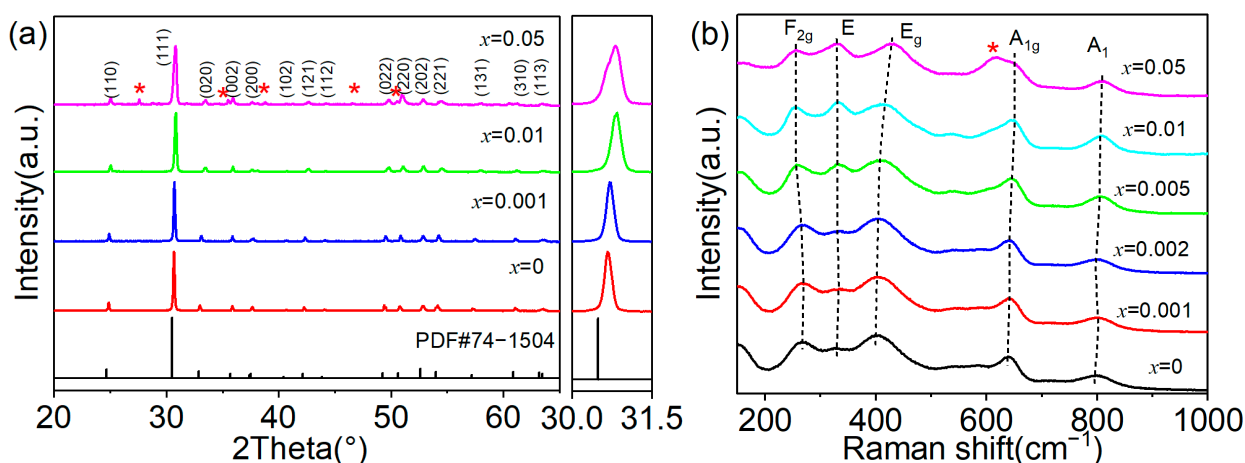


**Figure 1.** (a) XRD patterns of  $\text{Zr}_{1-x}\text{Eu}_x\text{TiO}_4$  ( $x = 0, 0.001, 0.01, 0.05$ ) samples. (b) Raman spectra of  $\text{Zr}_{1-x}\text{Eu}_x\text{TiO}_4$  ( $x = 0, 0.001, 0.002, 0.005, 0.01, 0.05$ ) samples. The dashed lines are drawn to guide the eye.

Raman spectroscopy is a powerful tool to determine the phase compositions of many transition metal oxides; herein, this technique was employed to distinguish the phase purity of the samples as prepared. In term of the space group of  $Pbcn-D_{2h}^{14}$ , 18 Raman-active could be predicted for  $\text{ZrTiO}_4$  [14,35]. However, only 12 Raman bands are generally observed. As shown in Figure 1b, in our samples, only five bands were significantly distinguished in the range of 200–1000  $\text{cm}^{-1}$  due to their occurrence at lower wavenumbers, their overlapping of the band, or due to them being too weak to be observed for the unobserved modes/bands. The three bands centered at 640, 404, and 267  $\text{cm}^{-1}$  are attributed to vibrational modes  $A_{1g}$ ,  $E_g$ , and  $F_{2g}$ , respectively, of  $\text{Ti}(\text{Zr})\text{O}_6$  octahedron, and the two bands at 327 and 799  $\text{cm}^{-1}$  are considered to arise from vibration modes  $E$  and  $A_1$ , respectively, of  $\text{Ti}(\text{Zr})\text{O}_4$  [14,35]. A clear shift of the Raman band with the higher  $\text{Eu}^{3+}$  concentration was found upon taking a closer look—particularly, the  $F_{2g}$  mode shifted to lower wavenumbers while  $A_{1g}$  and  $E_g$  moved to a higher frequency region when increasing the  $x$  value. In addition, an extra band appeared at 602  $\text{cm}^{-1}$  for the  $\text{Zr}_{0.95}\text{Eu}_{0.05}\text{TiO}_4$ . Such spectral evolutions could be interpreted as being due to the presence of lattice distortion and impurity constituents caused by  $\text{Eu}^{3+}$  doping, which results in the variation of bond length and/or force constant of bond. These results coincided with the above analysis by XRD.

Figure 2 depicts the SEM images of the obtained samples. For the pristine  $\text{ZrTiO}_4$ , a single particle is characteristic of a quasi-sphere shape and has a size in the range of  $\sim 0.6$ – $1$   $\mu\text{m}$ . Some neighboring particles are connected through necks and exhibit dendritical growth from the nucleation centers. It was found that the starting materials of  $\text{Eu}_2\text{O}_3$  played another role of sintering flux and favored the growth of  $\text{ZrTiO}_4$  crystallites. Upon increasing the  $\text{Eu}^{3+}$  concentration, the size of the resulting phosphors constantly increased and approached to  $\sim 2$   $\mu\text{m}$  or more at  $x \geq 0.01$ ; serious agglomeration and more irregular morphology were clearly observed at higher  $\text{Eu}^{3+}$  concentrations. Surface diffusion and grain boundary diffusion of the various elements in the samples, which mainly controlled the formation and growth of the sintering necks, is expected to cause significant

changes in the size and morphology during high-temperature calcinations [37,38]. It is apparent that additions of a small amount of  $\text{Eu}_2\text{O}_3$  enhanced such microscopic diffusion processes, and then drove the solid-state reaction of different starting materials; further aggregation/coalescence and growth of crystallites thus arose.

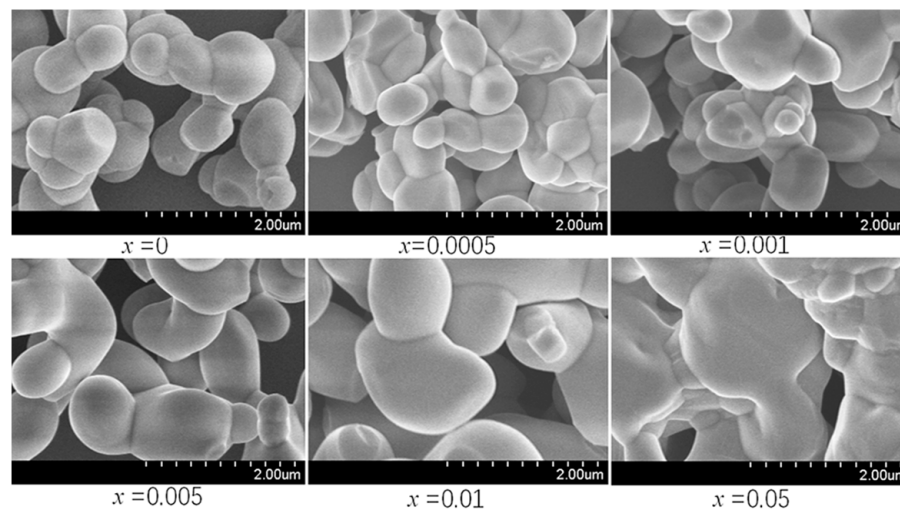


**Figure 2.** SEM images of the as-prepared  $\text{Zr}_{1-x}\text{Eu}_x\text{TiO}_4$  ( $x = 0, 0.0005, 0.001, 0.005, 0.01, 0.05$ ) phosphors.

### 3.2. Electronic Band Structure of $\text{Zr}_{1-x}\text{Eu}_x\text{TiO}_4$

In the systems of oxides typically containing closed-shell TM ions ( $\text{TM}^{4+/5+/6+}$ ,  $nd^0$ ) and oxygen anions ( $\text{O}^{2-}$ ,  $2p^6$ ), including simple binary compounds (e.g.,  $\text{TiO}_2$ ,  $\text{ZrO}_2$ ,  $\text{Nb}_2\text{O}_5$ ,  $\text{Ta}_2\text{O}_5$ ,  $\text{WO}_3$ ) and ternary compounds (various titanates, niobates, tantalates, tungstates and molybdates), their band gaps are commonly of ligand-metal CT type with the character of the upper part of the valence band (VB) mainly constituted with the oxygen 2p states, while the bottom of the conduction band (CB) is predominantly formed by the empty d states of the TM ions [39–41]. The fundamental optical absorption across the band gap occurs in the  $\text{TMO}_x$  complex polyhedron, involving an optical excitation of electrons from one of the highest filled molecular orbitals, which are localized on the  $\text{O}^{2-}$  ions (2p orbitals), to one of the lowest empty molecular orbitals, which are mainly localized on the  $\text{TM}^{4+/5+/6+}$  ion ( $t_{2g}$  orbital) [39–41]. For  $\text{ZrTiO}_4$ , as demonstrated above, it comprises two types of closed-shell TM ions ( $3d^0/\text{Ti}^{4+}$ ,  $4d^0/\text{Zr}^{4+}$ ) and then two kinds of  $\text{TMO}_6$  octahedra ( $\text{TiO}_6/\text{ZrO}_6$ ), so the band gap was also considered to be the charge transfer type of  $\text{O}^{2-} \rightarrow \text{Ti}^{4+}$  or  $\text{O}^{2-} \rightarrow \text{Zr}^{4+}$ . It is worthwhile to note that the fourth ionization potential (Coulomb binding energy) of  $\text{Ti}^{4+}$  (43.27 eV) is  $\sim 8.93$  eV higher in energy than that of  $\text{Zr}^{4+}$  (34.34 eV) [42]. According to the model suggested by Blasses et al. [39–41], the band gap should be mainly of the  $\text{O}^{2-} \rightarrow \text{Ti}^{4+}$  CT type. Such an inference was confirmed by the DFT calculation on the electronic structure of  $\text{ZrTiO}_4$  recently made by E. Giamello et al. [7], which further indicated that  $\text{ZrTiO}_4$  has the nature of the direct band gap.

The band gap of  $\text{ZrTiO}_4$  was calculated according to Tuac's method [43]; the absorption coefficient  $\alpha$  for the direct band gap materials is given by:

$$(\alpha \cdot h\nu) = B(h\nu - E_g)^m \quad (2)$$

where  $h$  is the Planck constant,  $\nu$  is the frequency of photon,  $E_g$  is the band gap energy,  $B$  is an energy independent constant, and  $m$  is an index that depends on the nature of electronic transition responsible for the optical absorption. The value of  $m$  for the allowed direct transition is 0.5. For powdered samples, usually only the diffuse reflectance spectra

could be measured; an inverse relation between the reflectance and absorption enables the  $\alpha$  to be approximately given using the Kubelka–Munk function [44]:

$$\frac{\alpha}{S} \approx F(R) = \frac{(1 - R)^2}{2R} \quad (3)$$

where R is the reflectance of an infinitely thick specimen; S is defined as the scattering factor, which becomes constant when the thickness of the sample is much larger than the size of the individual particles. The absorption spectra ( $F(R)$ ) of  $Zr_{1-x}Eu_xTiO_4$  against wavelengths were shown in Figure 3, where a steep optical absorption edge followed by a peak at  $\sim 320$  nm was observed for  $ZrTiO_4$ . The optical band gap energy for  $ZrTiO_4$  was evaluated to be  $\sim 3.65$  eV ( $\sim 340$  nm) with Tauc's plot (the inset of Figure 3), which is analogous to previous reports [7,14,45].

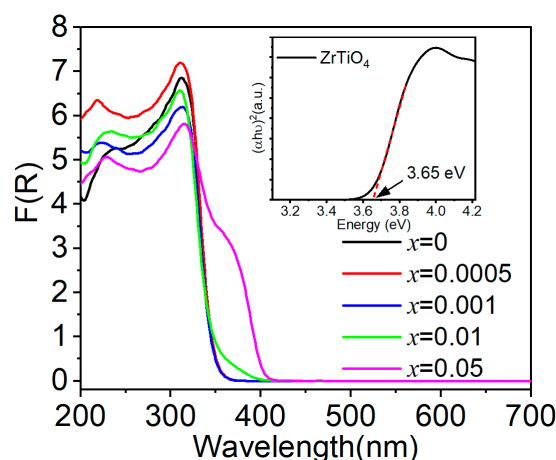


**Figure 3.** Absorption spectra ( $F(R)$ ) of  $Zr_{1-x}Eu_xTiO_4$  ( $x = 0, 0.0005, 0.001, 0.01, 0.05$ ). In the inset is the Tauc's plot of  $ZrTiO_4$ , a linear extrapolation of the steep slope in the curve to the X-axis was used to determine the band gap energy.

In addition, an extra absorption band lying well in the transparent region of crystal (i.e., below the absorption edge, see Figure 3) could be distinguished for the samples doped with  $Eu^{3+}$  at concentration above  $x = 0.01$ , which dramatically intensified with the increase in  $Eu^{3+}$  concentration. At  $x = 0.05$ , the onset of the absorption has shifted from  $\sim 350$  nm for pure  $ZrTiO_4$  to  $\sim 404$  nm in the visible spectral region. This band should arise from the impurities or defects in the lattice matrix. As is well known, the introduction of  $Eu^{3+}$  impurities in one host lattice could give rise to additional absorption bands originating from the  $O^{2-} \rightarrow Eu^{3+}$  CT process and electronic transitions within the  $4f^6$  shell. However, the former was commonly characterized by a strong broad band in the higher energy of the ultraviolet (UV) region whereas the latter by weak and sharp peaks. The extra absorption band observed, therefore, arose from the defects. As demonstrated above,  $Eu^{3+}$  incorporation yielded extrinsic oxygen vacancies for charge compensation. Such defects were thus identified as oxygen vacancies; the absorption originated from the transition of electron from the top of the valence band to the defect levels lying below the bottom of the conduction band.

It is known that optical excitation across the band gap of the crystal lattice could yield free charge carriers (electron, hole) or electron-hole pairs (exciton), which is subject to the competition of two opposing interactions: delocalization and localization [46]. The delocalization of the excited state, i.e., energy band formation, would necessarily result in the lower energy position of the optical absorption edge [19,21,47]. This is well illustrated by the titanates following the decreased coupling strength between the titanate octahedra; some values of absorption edge have been reported and compared:  $TiO_2$  (rutile), 3.0 eV;  $SrTiO_3$ , 3.2 eV;  $MgTiO_3$ , 3.7 eV;  $BaTi(PO_4)_2$ , 3.8 eV, where the  $TiO_2$  is constituted with strongly coupled  $TiO_6$  octahedra and corresponds to one extreme of the formation of free exciton while the latter compound of  $BaTi(PO_4)_2$  contains completely isolated  $TiO_6$  octa-

hedra and corresponds to another extreme of the formation of self-trapped exciton [47]. For  $\text{ZrTiO}_4$ , the onset of the absorption edge is located at  $\sim 3.54$  eV (350 nm), which lies between these two extremes. We can thus conclude that the excited electrons upon excitation into the absorption edge show a large amount of delocalization. This could be understood from the structural features of  $\text{ZrTiO}_4$ . As demonstrated above, the  $\text{TiO}_6/\text{ZrO}_6$  octahedra (50%/50%) in the  $\text{ZrTiO}_4$  lattice are of random distribution and of edge-shearing. There must be a somewhat high probability to form some spatial areas comprising of only  $\text{TiO}_6$  octahedra or of a larger percentage of  $\text{TiO}_6$  octahedra inside, that is, some  $\text{TiO}_6$  may aggregate together and favor the strong three-dimensional coupling between them. As a consequence, the delocalization of excited electrons occurred.

### 3.3. Luminescence Properties of $\text{ZrTiO}_4$

Following the characteristics of optical absorption, the PL spectra of  $\text{ZrTiO}_4$  at room temperature were recorded upon excitation into the optical absorption edge (at 340 nm), above (at 300 nm) and below (at 430 nm) the band gap, respectively, as shown in Figure 4a. It was found that upon excitation into the optical absorption edge,  $\text{ZrTiO}_4$  shows a very weak yellow luminescence (see Figure 4b) characterized by a superbroad band (with the full width at the half maximum of 191 and 197 nm for 300 and 340 nm excitations, respectively) in the range of  $\sim 450$ – $800$  nm and a peak at  $\sim 570$  nm; while an analogous luminescence band in addition to a slight blue shift (peaking at  $\sim 550$  nm) was observed after excitation above the band gap. For the excitation below the band gap, a much weaker red emission (with a peak at  $\sim 650$  nm) was observed. Since this excitation corresponds to the extrinsic absorption of the exciting radiation by the defect states, such emissions were thus attributed to the defect-mediated luminescence. In contrast, the difference in spectral profiles enabled us to preliminarily assign the luminescence under intrinsic excitation to host emissions.

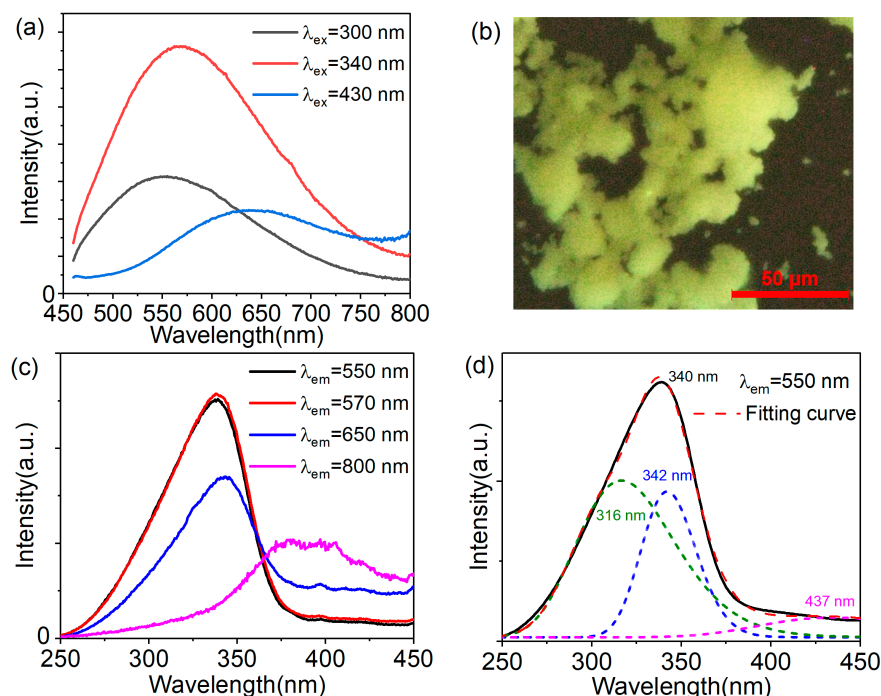


**Figure 4.** (a) Emission and (c,d) excitation spectra of the luminescence of  $\text{ZrTiO}_4$  at room temperature. (b) Fluorescence microscopy image ( $200\times$ ) of  $\text{ZrTiO}_4$  under excitation of 340–370 nm.

The identity of such defects was considered to be oxygen vacancies, arising from the nonstoichiometry of  $\text{ZrTiO}_4$  due to the reducibility of metal cations, especially the  $\text{Ti}^{4+}$  ions. The compound should undergo oxygen depletion under high temperature annealing, which more favorably occurred under low oxygen partial pressure or reducing atmo-



spheres. In fact, the starting materials of TiO<sub>2</sub> and ZrO<sub>2</sub> are both typical anion-vacancy-typed nonstoichiometric compounds. The reaction is represented by:



an oxygen ion in the lattice dissociates into a neutral oxygen atom, which leaves the crystal, and two electrons that are left behind. The presence of oxygen vacancies (neutral, singly, or doubly charged) enables the formation of donor levels under the bottom of the conduction band, which is positioned over a wider range in energy caused by the difference in charge and local environment.

Figure 4c depicts the excitation spectra of ZrTiO<sub>4</sub> emissions at different wavelengths. By monitoring the host-dominated emissions (550 and 570 nm), the excitation spectra almost overlap each other, where a broad asymmetric band with a sharp edge at long wavelengths side peaking at ~340 nm was observed, which was followed by a tail extending into the visible region. When monitoring the defects-dominated long-wave emissions (650 and 800 nm), the ratio of the tail to the main peak increased; an apparent peak at ~380 nm then appeared for 800 nm emission. It further indicated that undoped ZrTiO<sub>4</sub> could be excited by irradiation with energy below and above the band gap. The former mainly corresponds to the defects-mediated luminescence, while the latter yields the intrinsic host luminescence. The asymmetric nature of excitation spectra in the short-wave region was also observed in other titanate systems [21]. Upon Gaussian fitting, the excitation spectrum of ZrTiO<sub>4</sub> host emissions could be well decomposed into three sub-bands peaking at 316, 342, and 437 nm (denoted as G316, G342, and G437, respectively), as shown in Figure 4d. The two UV bands coincided with the host absorption, where free electrons in the conduction band could be created, which could bind with holes to form exciton states after fast lattice relaxation. Herein, the following yellow luminescence was ascribed to STEs recombination at defects sites as deep center emissions in view of the characteristics of the effective excitation not located in the transparent region of the crystals, superbroad band, and large Stokes shift (1.64 eV for 316 nm excitation and 1.45 eV for 342 nm excitation) [47]. The formation of STEs from free excitons was accompanied by a distortion of the lattice surroundings due to the strong electron-lattice coupling. This could be supported by the aforementioned microstructure features, including the random distribution of Ti(Zr)O<sub>6</sub> octahedra and intrinsic oxygen vacancies due to nonstoichiometry. In accordance with the electronic band structure, herein the STEs were suggested to occur in the TiO<sub>6</sub><sup>8-</sup> octahedra, of which the emissions were of the charge-transfer type. Alternatively, titanate luminescence in several other types of TiO<sub>x</sub> groups was previously reported [19–21].

As regard to two Gaussian sub-bands (G316 and G342 nm) in the short-wave region, they could be tentatively distinguished as two types of TiO<sub>6</sub><sup>8-</sup>—the isolated/ localized and coupled/delocalized ones, respectively. Note that the peak energy of shorter-wave constituent (316 nm, 3.90 eV) is in good agreement with the absorption of titanate groups in BaTi(PO<sub>4</sub>)<sub>2</sub>, where completely isolated TiO<sub>6</sub><sup>8-</sup> octahedra have been demonstrated [21]. In addition, it cannot be excluded that some intermediary situations occurred in the lattices by considering the coupling extent between the titanate groups or their amounts in the spatial regions of aggregation, of which the exact excitation peaks were situated between 316 and 342 nm.

In Figure S2, it is shown that the yellow luminescence was significantly intensified by a factor of 12 under the band gap excitation as the temperature decreased to 77 K. This could be interpreted as being due to the reduced nonradiative transitions in the titanate group which competes with the radiative transitions and the suppression of luminescence quenching via migration of STEs to the energy sinks present in the lattice. The mobility of STEs at lower temperature would be constrained due to the smaller thermal energy.

The fluorescence kinetics of ZrTiO<sub>4</sub> was studied at room temperature and 77 K. As shown in Figure 5a, the decay traces are nonexponential and closely follow each other upon

excitation at 300 and 340 nm. The decay curves could be well fitted by double exponential function ( $I = A_1 e^{-\frac{t}{\tau_1}} + A_2 e^{-\frac{t}{\tau_2}}$ , with the intensity  $I$ , different lifetime constants ( $\tau_1$ , a fast one;  $\tau_2$ , a slow one) and percentages of the initial intensity of each lifetime component ( $A_1$ ,  $A_2$ )), yielding shorter average lifetimes ( $\bar{\tau}$ ) of  $\sim 20.9$  ns by using the equation  $\bar{\tau} = \frac{A_1 \tau_1^2 + A_2 \tau_2^2}{A_1 \tau_1 + A_2 \tau_2}$  (see Table S1); At 77 K, however, the decays remarkably prolonged, as shown in Figure 5b and Table S1. The average lifetimes increased by three orders of magnitude and reached the microsecond scale ( $\sim 15.6$   $\mu$ s for isolated titanate groups at  $\lambda_{\text{ex}} = 300$  nm,  $\lambda_{\text{em}} = 550$  nm and  $\sim 37.2$   $\mu$ s for coupled titanate groups at  $\lambda_{\text{ex}} = 340$  nm,  $\lambda_{\text{em}} = 550$  nm), which coincided with the observation of the considerable increase in fluorescence intensity due to the reduced nonradiative transitions. The slightly faster fluorescence decay for isolated titanate groups was due to the larger Stokes shift than that of the coupled ones, which resulted in the smaller activation energy of thermal quenching according to the configuration coordinate model and then the increased nonradiative return from the excited to the ground state via the parabola crossover. In addition, the long lifetimes in the microsecond scale indicate that STEs in the studied  $\text{TiO}_6^{8-}$  groups have a triplet nature. The radiative recombination became (partly) forbidden by the spin selection rule, which slows down the optical transition rate. In contrast, decays of defect luminescence (see Figure 5b, Figure S3 and Table S1) are somewhat allowed with a shorter lifetime component in the the nanosecond scale, even at 77 K. The significant difference in fluorescence kinetics further supported the above assignment of the luminescence to the defect and intrinsic STEs states. A host-referred binding energy scheme for defect and intrinsic STEs states, as well as the related absorption/excitation and luminescent process in  $\text{ZrTiO}_4$ , was shown in Figure 6.

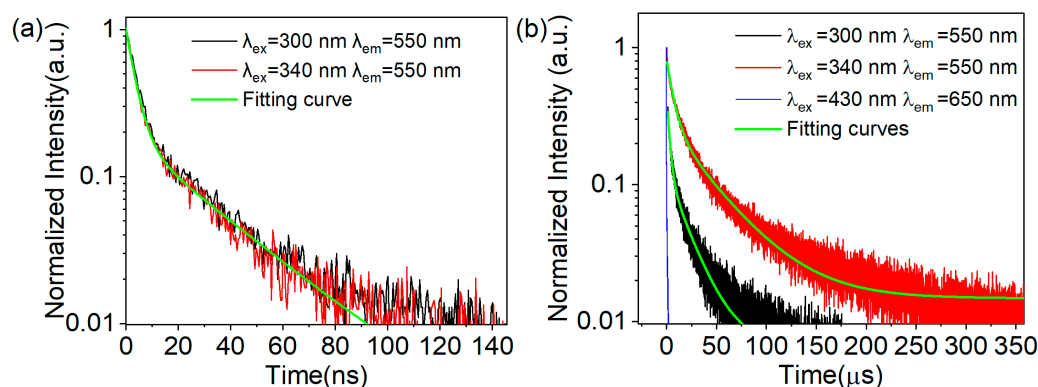


**Figure 5.** Fluorescence decays of  $\text{ZrTiO}_4$  at room temperature (a) and 77 K (b); The excitation and emission wavelengths for each decay measurement were indicated.

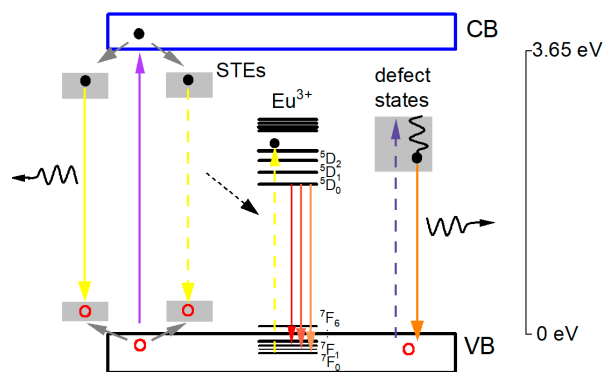


**Figure 6.** The host-referred binding energy scheme for the STE state, the  $\text{Eu}^{3+}$  ions and defect state together with their absorption/excitation, related energy transfer, and luminescence processes in  $\text{ZrTiO}_4$ .

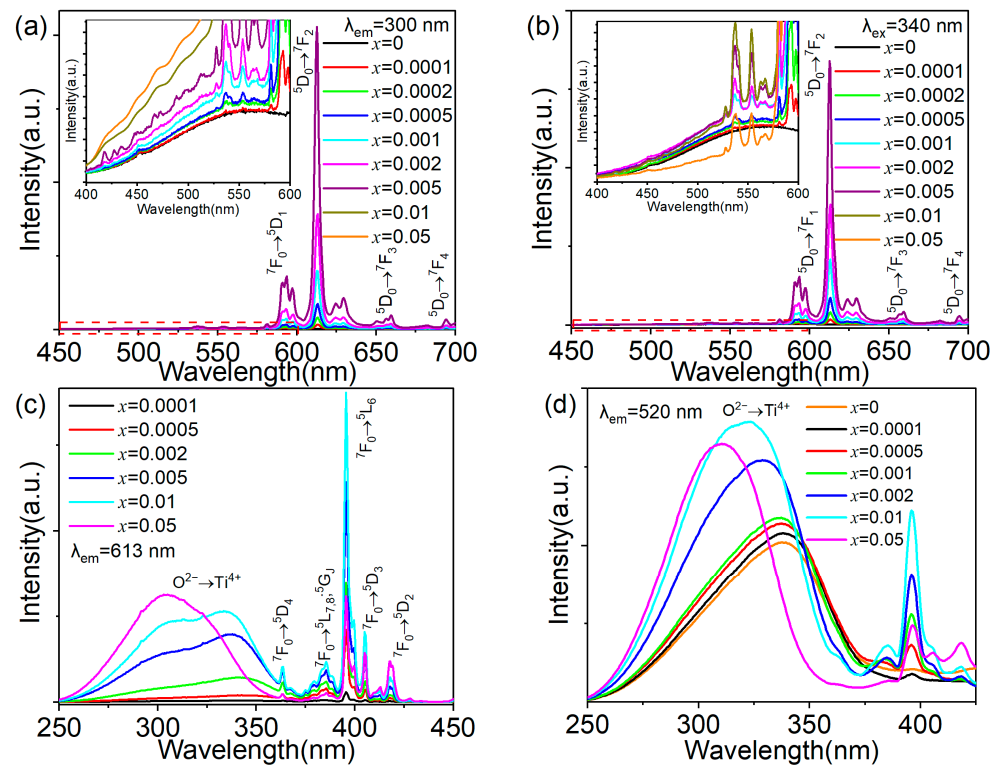
### 3.4. Luminescence Properties of $Zr_{1-x}Eu_xTiO_4$

Figure 7a,b show the emission spectra of  $Zr_{1-x}Eu_xTiO_4$  under band gap excitation. The emission of these phosphors exhibits the well-known  $Eu^{3+}$  emission lines from the  $^5D_0$  level to the  $^7F$  manifold, which do not need a further assignment. The availability of a low symmetry of a site as  $C_2$  without a reversion center for  $Eu^{3+}$  in  $ZrTiO_4$  leads to the more intense red emissions arising from  $^5D_0 \rightarrow ^7F_2$  forced electronic dipole transitions than the orange emissions originating from  $^5D_0 \rightarrow ^7F_1$  magnetic dipole transitions due to the breakdown of parity prohibition by the odd crystal-field term [48,49]. Noteworthy are the  $Eu^{3+}$  sharp emissions that are much stronger than the broadband STEs emissions, a continuous increase rather than decrease in the luminescence intensity of STEs with higher  $Eu^{3+}$  concentration for excitation at 300 nm, and the first increase and then decrease in STEs emissions for excitation at 340 nm (see the insets in Figure 7a,b and Figure S4). The excitation spectra of the  $Eu^{3+}$  fluorescence of phosphors  $Zr_{1-x}Eu_xTiO_4$  are given in Figure 7c. The sharp lines are the intraconfigurational transitions of the  $4f^6$  configuration of the  $Eu^{3+}$  ion; the broad bands in the UV region correspond well with the optical absorption observed in the reflection spectrum and show an asymmetric profile analogous to that of the STEs excitation bands shown in Figure 4c—it is therefore due to host excitation (titanate groups). This shows that effective host sensitized energy transfer takes place from both isolated and coupled titanates (corresponding to the G316 and G342 sub-bands in Figure 4d, respectively) to europium ions. Although the STEs luminesced weakly at room temperature and most of the excitation energy dissipated via exciton migration to quenching centers (as illustrated in preceding section), they still could serve as donors and effectively sensitize the  $Eu^{3+}$  luminescence. At room temperature, the principal luminescence is the red emissions for sample  $Zr_{0.99}Eu_{0.01}TiO_4$  under 340–370 nm excitation (see Figure S5); it appeared that  $Eu^{3+}$  ions were much more effective in trapping the mobile excitons than the other quenchers. In addition, the transfer time to  $Eu^{3+}$  must be shorter than the hopping time of the exciton, that is, the average energy transfer rate to  $Eu^{3+}$  is much higher. An important suggested factor is that the  $Eu^{3+}$  ions are prone to situate in the vicinity of isolated titanate groups or to enter in the spatial area of coupled titanates, whereas the quenchers are not, since the energy transfer/migration is of distance dependence. Host-sensitized energy transfer to  $Eu^{3+}$  was schematically shown in Figure 6.

In the presence of the acceptor of  $Eu^{3+}$ , the continuous increase in the luminescence intensity of STEs as donors was anomalous, because the nonradiative energy transfer from the donor to acceptor commonly degrades the donor luminescence. Such an anomalous phenomenon was further confirmed by the excitation spectra of STEs emissions of samples doped with different concentration of  $Eu^{3+}$ . As shown in Figure 7d, upon monitoring the 520 nm emission at which the interference of luminescence from  $Eu^{3+}$  was significantly reduced, it was found that the broad band of host excitation intensified with a higher  $Eu^{3+}$  concentration in the range  $x = 0\text{--}0.002$  while keeping the spectral profile constant. At much higher concentrations, the band became narrow, accompanied by a peak shift to the short-wave side. This actually arose from the evolution of the relative intensity of such two spectral constituents, where the G316 constituent enhanced with the higher  $Eu^{3+}$  concentration while the G342 band weakened continuously. At  $x = 0.05$ , the latter almost disappeared and only the former was left behind. Returning to the excitation spectra of  $Eu^{3+}$  emissions in Figure 7c, a similar evolution of the spectral profile was also observed in this part of the broad band. In the  $Eu^{3+}$  concentration range under investigation, the fraction of G316 constituent increased gradually, while from  $x = 0.01$  to 0.05, the fraction of G342 sub-band significantly decreased.

Three factors were considered to account for the above results. Given the fact that  $Eu^{3+}$  doping produced an amount of defect states below the conduction bottom, and their optical absorption shared the same electrons from O 2p levels at the top of valence band with fundamental absorption, the first factor is thus the competitive absorption occurrence between the defect states and host conduction band in the spectral region of the absorption edge. The electron transitions from the top of the valence band to the defect states

were considered to be more competitive, and the fraction of exciting irradiation being absorbed via fundamental process was then reduced; thus, it suppressed/eliminated the effective band gap excitations belong to the G342 constituent. This factor favors the observation on the significant degradation of the G342 constituent present in the excitation spectra of both STEs and  $\text{Eu}^{3+}$  emissions when doping with higher concentration of  $\text{Eu}^{3+}$  (see inset of Figure 7c,d). The competitive absorption also occurred in the near UV region (375–410 nm) between the defect-mediated process and electronic transitions within the  $4f^6$  shell of  $\text{Eu}^{3+}$ . As shown in Figure 7c, the excitation intensity of  ${}^7\text{F}_0 \rightarrow {}^5\text{D}_3$ ,  ${}^5\text{L}_6$ ,  ${}^5\text{G}_J$ ,  ${}^5\text{D}_4$  transitions dramatically decreased when the doping concentration of  $\text{Eu}^{3+}$  increased from  $x=0.01$  to  $0.05$ , while the excitation line of  ${}^7\text{F}_0 \rightarrow {}^5\text{D}_2$  transition ( $\sim 465$  nm), located outside the defect-mediated absorption region, increased in succession (see Figure S6). Another factor is the increased amounts of isolated  $\text{TiO}_6$  octahedra driven by  $\text{Eu}^{3+}$  doping. As suggested above, the  $\text{Eu}^{3+}$  dopants may enter the spatial area comprising aggregated  $\text{TiO}_6$  octahedra, which would break the interactions between them and produce more isolated  $\text{TiO}_6$  octahedra. This factor especially favors the continuous enhancement, with increased  $\text{Eu}^{3+}$  concentration of the G316 constituent present in the excitation of STEs emissions (see inset of Figure 7a,d). The third is the energy back-transfer from  $\text{Eu}^{3+}$  activators to other titanate groups, which could emit more efficiently than such donors actioned in the first step of sensitized process. It favors the observation on the continuous enhancement, in the low  $\text{Eu}^{3+}$  concentration range, of the whole broad band present in the excitation spectra of STEs emissions (see Figure 7d). Depending on the  $\text{Eu}^{3+}$  concentration, the above factors are each expected to function dominantly in different samples.



**Figure 7.** (a,b) Emission spectra of  $\text{Zr}_{1-x}\text{Eu}_x\text{TiO}_4$  ( $x = 0, 0.0001, 0.0005, 0.002, 0.005, 0.01, 0.05$ ) phosphors upon host excitation ( $\lambda_{\text{ex}} = 300$  and  $340$  nm); (c,d) Excitation spectra of  $\text{Zr}_{1-x}\text{Eu}_x\text{TiO}_4$  ( $x = 0, 0.0001, 0.0005, 0.002, 0.005, 0.01, 0.05$ ) phosphors of  $\text{Eu}^{3+}$  emissions ( $\lambda_{\text{em}} = 613$  nm) and STEs emissions ( $\lambda_{\text{em}} = 520$  nm). The inset is a zoomed view of the area shown by a rectangle in the figure.

The fluorescence decays of  ${}^5\text{D}_0$  level of  $\text{Eu}^{3+}$  were measured at room temperature upon excitation into the  ${}^5\text{D}_1$  level ( $\lambda_{\text{ex}} = 534$  nm,  $\lambda_{\text{em}} = 613$  nm) (see Figures 8 and S7). Following the increase in  $\text{Eu}^{3+}$  concentration, the decay could be distinguished by two regions

with an abrupt lifetime extension between  $x=0.001$  and  $0.002$ . In each region, the decays are almost independent of  $\text{Eu}^{3+}$  concentration. Another feature is that the decay slightly deviated from single exponential at a lower concentration ( $x \leq 0.001$ ), but more closely followed the single exponential at a higher concentration ( $0.002 \leq x \leq 0.05$ ); particularly at  $x = 0.05$ , the decay became pure exponential with a  $1/e$  value of  $\sim 0.73$  ms. This behavior is anomalous for trivalent  $\text{Ln}^{3+}$  ions, since a nonexponential decay was commonly observed at higher concentrations due to concentration quenching. Herein, it is considered that energy back-transfers from the lowest excited state of  $^5\text{D}_0$  level of  $\text{Eu}^{3+}$  to host lattice (titanate groups) are responsible for the faster and nonexponential decay at lower  $\text{Eu}^{3+}$  concentrations, at which concentration isolated  $\text{Eu}^{3+}$  are preferentially formed in close connection with the surrounding titanate groups. Such an energy back-transfer was possible by considering the superbroad character of STEs luminescence and large spectral overlapping between the luminescence of  $\text{Eu}^{3+}$  and STEs. It should occur from  $^5\text{D}_0$  level to the spin-forbidden emitting level of STEs. Nevertheless, the  $\text{Eu}^{3+}$  ions tend to aggregate into clusters in the lattice at higher concentration due to the aliovalent substitution on the tetravalent sites, where the interaction between  $\text{Eu}^{3+}$  ions and the titanate groups of hosts weakened but enhanced with themselves. Under this circumstance, the energy back-transfer from the guest of  $\text{Eu}^{3+}$  to the host was then suppressed/ reduced, and an extended lifetime of the emitting level thus arose. These results coincided with the above observation on the anomalous increase in STEs luminescence with a higher doping concentration.

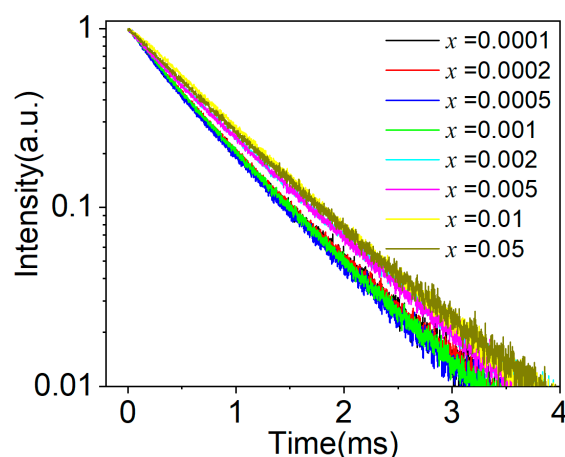


**Figure 8.** Fluorescence decay curve of  $^5\text{D}_0$  level  $\text{Eu}^{3+}$  ions in  $\text{Zr}_{1-x}\text{Eu}_x\text{TiO}_4$  ( $x = 0.0001, 0.0002, 0.0005, 0.001, 0.002, 0.005, 0.01, 0.05$ ) ( $\lambda_{\text{ex}} = 534$  nm  $\lambda_{\text{em}} = 613$  nm).

### 3.5. Optical Thermometry

As demonstrated in the preceding section, energy transfer-derived dual-emissions were observed in  $\text{Zr}_{1-x}\text{Eu}_x\text{TiO}_4$  phosphors upon host excitation—the yellow STEs and red  $\text{Eu}^{3+}$  emissions. There is delocalization for STEs at elevated temperatures and quenching centers are easily reached, so that the quantum efficiency becomes low at room temperature. For  $\text{Eu}^{3+}$ , given that fact that it could be effectively sensitized by the host lattice, including nearby and migrated STEs and the well-shielded character of the 4f electrons, the resulting luminescence from  $4f^6-4f^6$  electronic transitions is expected to be somewhat stable against temperature.  $\text{Zr}_{1-x}\text{Eu}_x\text{TiO}_4$  phosphors thus have promising potential for developing high performance ratiometric self-referencing optical thermometry upon single wavelength excitation, with STEs luminescence as temperature signals and  $\text{Eu}^{3+}$  luminescence as internal reference. Towards the high signal discriminability required for both working and reference signals, a lower concentration of  $\text{Eu}^{3+}$  doping was chosen to attain the temperature sensing by considering the effective luminescence of  $\text{Eu}^{3+}$  itself and luminescence quenching of STEs induced by defects stated as being produced upon heavy doping of  $\text{Eu}^{3+}$ . In the following, the temperature dependence (153–313 K) of luminescence of typical  $\text{Zr}_{1-x}\text{Eu}_x\text{TiO}_4$  ( $x = 0.0001$ ) phosphor was examined upon 340–370 nm ex-

citation for temperature sensing, as shown in Figure 9a. In view of the feature of spectral overlapping between STEs and  $\text{Eu}^{3+}$  and the necessity of avoiding the interference from  $\text{Eu}^{3+}$  luminescence, the luminescence in a spectral region of 500–570 nm was extracted as signals for STEs ( $I_{\text{STEs}}$ ). The luminescence in the range of 609–612 nm was detected for  $\text{Eu}^{3+}$  ( $I_{\text{Eu}}$ ), which actually involved emissions from both STEs and  ${}^5\text{D}_0\text{--}{}^7\text{F}_2$  transitions of  $\text{Eu}^{3+}$ . Temperature-dependent integrated intensity in such spectral regions is calculated according to:

$$I_{\text{STEs}} = \int_{500}^{570} I(\lambda, T) d\lambda \quad (5)$$

$$I_{\text{Eu}} = \int_{609}^{612} I(\lambda, T) d\lambda \quad (6)$$

where  $\lambda$  is the wavelength, and  $T$  is the corresponding temperature. A histogram of the integrated intensity was shown in Figure 9b. Impressively, the signals from STEs weakened quickly with an increase in temperature, whereas the signals from  $\text{Eu}^{3+}$  decreased much more slowly. At 153 K, the STEs signals were much higher than those of  $\text{Eu}^{3+}$ , whereas at 313 K, the STEs signals were almost quenched and those of  $\text{Eu}^{3+}$  remained. A remarkable change in FIR ( $I_{\text{STEs}}/I_{\text{Eu}}$ ) was thus attained against temperature, which follows the equation:

$$\text{FIR} = \frac{I_{\text{STEs}}}{I_{\text{Eu}}} = \frac{\int_{500}^{570} I(\lambda, T) d\lambda}{\int_{609}^{612} I(\lambda, T) d\lambda} = \frac{A}{1 + B \times \exp\left(-\frac{C}{T}\right)} + D \quad (7)$$

where  $A$ ,  $B$ ,  $C$  and  $D$  are constants. As shown in Figure 10a, the calculated FIR ( $I_{\text{STEs}}/I_{\text{Eu}}$ ) values could be approximated well by the fit using Equation (7), which could be specifically written as  $\text{FIR} = \frac{9.47}{1 + 3520 \times e^{-\frac{1973}{T}}} + 2.51$ . Two parameters for evaluating and comparing the performance of optical thermometric materials are absolute sensitivity ( $S_a$ ) and relative sensitivity ( $S_r$ ), which can be expressed as [22]:

$$S_a = \left| \frac{d(\text{FIR})}{dT} \right| = \frac{6.58 \times 10^7 \times e^{-\frac{1973}{T}}}{\left[ T \times \left( 1 + 3520 \times e^{-\frac{1973}{T}} \right) \right]^2} \quad (8)$$

$$S_r = 100\% \times \frac{1}{\text{FIR}} \left| \frac{d(\text{FIR})}{dT} \right| = 100\% \times \frac{6.58 \times 10^7 \times e^{-\frac{1973}{T}}}{\left( 11.98 \times e^{-\frac{1973}{T}} + 8835 \right) \times \left( e^{-\frac{1973}{T}} + 3520 \right) \times T^2} \quad (9)$$

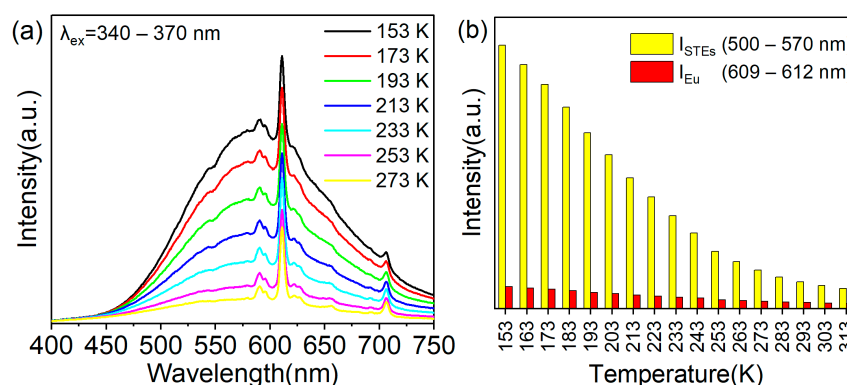


**Figure 9.** (a) Temperature-dependent PL spectra ( $\lambda_{\text{ex}} = 340\text{--}370$  nm) of the  $\text{Zr}_{1-x}\text{Eu}_x\text{TiO}_4$  ( $x = 0.0001$ ) phosphors recorded from 153 to 313 K (b) Temperature-dependent integrated spectral intensity for the STEs signals ( $I_{\text{STEs}}$ ) (500–570 nm) and  $\text{Eu}^{3+}$  signals (609–612 nm) ( $I_{\text{Eu}}$ ).

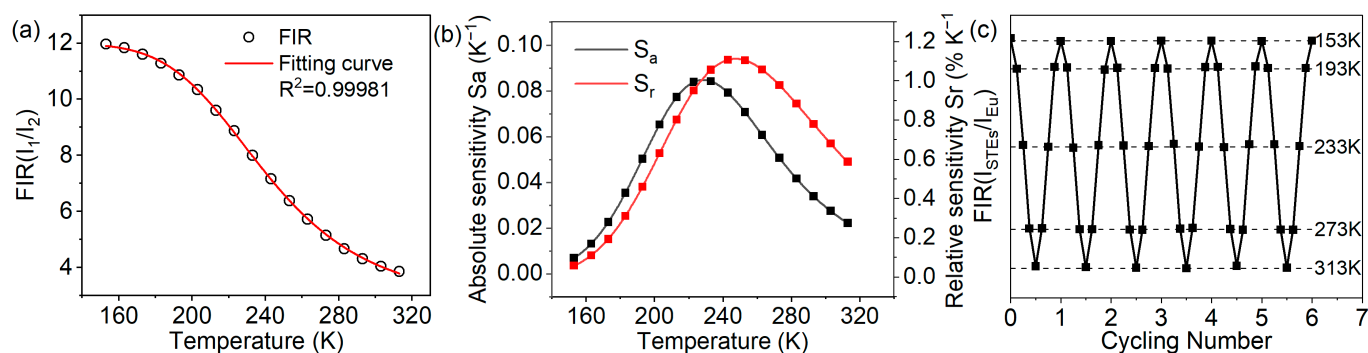


**Figure 10.** (a) Temperature dependence of the experimental FIR ( $I_{\text{STES}}/I_{\text{Eu}}$ ) values and the fitting curves using Equation (7) (b) Absolute sensitivity value  $S_a$  and relative sensitivity value  $S_r$  at different temperatures. (c) Temperature-induced switching of the FIR between the STEs signals ( $I_{\text{STES}}$ ) (500–570 nm) and  $\text{Eu}^{3+}$  signals (609–610 nm) ( $I_{\text{Eu}}$ ) (alternating between 153 K and 313 K).

Note that the  $S_r$  involves the variations of FIR value and absolute sensitivity  $S_a$  with respect to the temperature, which is independent of the nature of the thermometer, and was alternatively adopted in an effort to compare broad categories of temperature sensors [22]. Using Equations (8) and (9), the  $S_a$  and  $S_r$  parameters were determined and plotted in Figure 10b. The maximal  $S_a$  and  $S_r$  of the  $\text{Zr}_{1-x}\text{Eu}_x\text{TiO}_4$  ( $x = 0.0001$ ) sensing materials were  $0.08 \text{ K}^{-1}$  (at 233 K) and  $1.11\% \text{ K}^{-1}$  (at 243 K), respectively.

Table 1 compiled the related optical parameters of several representative optical thermometric materials on the basis of FIR strategy of dual-emitting centers. It can be seen that the maximal  $S_a$  and  $S_r$  values in this work are comparable with those of some materials.

**Table 1.** Optical parameters of several typical temperature sensing materials.

Materials	Luminescent Ions for Sensing	Excitation Wavelength (nm)	Maximum $S_a$ ( $\text{K}^{-1}$ )	Maximum $S_r$ ( $\% \text{K}^{-1}$ )	Temperature Range (K)	Ref.
$\text{LiLaP}_4\text{O}_{12}$	$\text{Tm}^{3+}$ , $\text{Eu}^{3+}$	975	-	1.8	123–473	[25]
$\text{Sr}_3\text{P}_4\text{O}_{13}$	$\text{Eu}^{2+}$ , $\text{Eu}^{3+}$	360	0.008	1.06	293–573	[26]
$\text{GdPO}_4: \text{Mn}^{2+}$ , $\text{Eu}^{3+}$	$\text{Mn}^{2+}$ , $\text{Eu}^{3+}$	375	-	8.88	303–323	[27]
$\text{NaLaMgWO}_6: \text{Er}^{3+}$	$\text{Er}^{3+}$	378	0.0223	1.04	303–483	[50]
$\text{La}_2\text{MgTiO}_6: \text{Pr}^{3+}$	$\text{Pr}^{3+}$	350	0.072	1.28	80–500	[51]
$\text{ZnGa}_2\text{O}_4: \text{Cr}^{3+}$ , $\text{Bi}^{3+}$	$\text{Cr}^{3+}$ , $\text{Bi}^{3+}$	430	-	1.93	293–473	[52]
$\text{BaAl}_{12}\text{O}_{19}: \text{Eu}^{2+}$ , $\text{Cr}^{3+}$	$\text{Eu}^{2+}$ , $\text{Cr}^{3+}$	325	0.0143	0.466	290–480	[53]
$\text{Na}_2\text{GdMg}_2(\text{VO}_4)_3$	$\text{Yb}^{3+}$ , $\text{Er}^{3+}$	980	0.749	0.976	303–573	[54]
$\text{CaTiO}_3: \text{Ti}^{3+}$ , $\text{Yb}^{3+}$	$\text{Ti}^{3+}$ , $\text{Yb}^{3+}$	266	0.311	3.55	77–480	[55]
$\text{GaTi}_2\text{O}_7: \text{Eu}^{3+}$	Traps $\text{Eu}^{3+}$	-	-	0.46	313–423	[36]
$\text{LiTaO}_3: \text{Ti}^{4+}$ , $\text{Eu}^{3+}$	$\text{Ti}^{4+}$ , $\text{Eu}^{3+}$	270	0.671	3.395	303–443	[35]
$\text{ZrO}_2: \text{Ti}^{4+}$ , $\text{Eu}^{3+}$	$\text{Ti}^{4+}$ , $\text{Eu}^{3+}$	280	0.414	3.84	303–413	[22]
$\text{ZrTiO}_4: \text{Eu}^{3+}$	$\text{Eu}^{3+}$ , $\text{Ti}^{4+}$	340	0.084	1.11	153–313	This work

Temperature uncertainty (or resolution)  $\delta_T$  is an important parameter to evaluate the accuracy of thermometers. It can be valued by the following Equation (10) [19,21]:

$$\delta T = \frac{1}{S_r} \frac{\delta \text{FIR}}{\text{FIR}} \quad (10)$$

As shown in Figure S8, the present optical thermometric material of  $\text{Zr}_{1-x}\text{Eu}_x\text{TiO}_4$  ( $x = 0.0001$ ) has a high resolution within 0.0016–0.2182 K in the temperature range of 153–313 K, indicating a high precision towards temperature sensing. The repeatability and reversibility of this thermometry was checked through six cycling experiments. The FIR at specific temperature is plotted in Figure 10c. It can be seen that the data points only show

a small deviation from the average values (dashed lines) for schemes, indicating a high durability and reproducibility for optical thermometry.

#### 4. Conclusions

In summary, orthorhombic  $\text{ZrTiO}_4$  and  $\text{ZrTiO}_4:\text{Eu}^{3+}$  phosphors were prepared by a solid-state reaction method, and their composition, structure, morphology, and optical properties were characterized by various techniques. The results indicated that the fundamental optical absorption edge of  $\text{ZrTiO}_4$  is of  $\text{O}^{2-} \rightarrow \text{Ti}^{4+}$  CT type and shifts to the long-wave side due to a large amount of delocalization of the excited state. Two types of  $\text{TiO}_6$  octahedra, the isolated/localized and coupled/delocalized, coexisted in the  $\text{ZrTiO}_4$  host matrix. Some spatial areas comprising only or a larger percentage of  $\text{TiO}_6$  octahedra were suggested to form towards the strong three-dimensional coupling between them, which favor the delocalization. It was found that  $\text{Eu}^{3+}$  doping induced the distortion of the lattice and produced oxygen vacancy defect states below the bottom of the conduction band.

In undoped  $\text{ZrTiO}_4$ , bright yellow luminescence of STEs recombination at defect sites was observed at low temperature under conditions of band gap excitation, but this was greatly decreased at room temperature due to the thermally activated STEs migration to quenching centers. Weak red luminescence from oxygen defects appeared when exciting into the transparent region of crystals. In  $\text{ZrTiO}_4:\text{Eu}^{3+}$  phosphors, effective host sensitized energy transfer to  $\text{Eu}^{3+}$  was observed and yielded the red characteristic emissions of  $\text{Eu}^{3+}$ . Anomalous STEs luminescence enhancement and spectral blue-shift in the excitation spectra with higher  $\text{Eu}^{3+}$  doping concentration were found and explained upon considering three factors: competitive absorption between electron transitions from the top of the valence band to the defect states and host conduction band,  $\text{Eu}^{3+}$  doping-driven production of more isolated  $\text{TiO}_6$  octahedra, and energy back-transfer from  $\text{Eu}^{3+}$  activators to other titanate groups emitting more efficiently, which was supported by the studies on decay kinetics of  $\text{Eu}^{3+}$ .

Due to the dramatic thermal quenching of STEs luminescence  $\text{ZrTiO}_4:\text{Eu}^{3+}$  phosphors were demonstrated to be ratiometric self-referencing optical temperature sensing materials on the basis of a dual-emitting combination strategy.  $\text{Zr}_{1-x}\text{Eu}_x\text{TiO}_4$  ( $x = 0.0001$ ) phosphor was selected as a proof of concept for the optical thermometry. The FIR ( $I_{\text{STEs}}/I_{\text{Eu}}$ ) was extracted by using the luminescence in a selective spectral region of 500–570 nm for STEs signals ( $I_{\text{STEs}}$ ) and that in spectral region of 609–612 nm for  $\text{Eu}^{3+}$  ( $I_{\text{Eu}}$ ), which closely follows the Arrhenius-type Mott equation in the working range of 153–313 K. The maximum relative sensitivity amounts to  $\sim 1.1\% \text{K}^{-1}$  at 243 K.

**Supplementary Materials:** The following supporting information can be downloaded at: <https://www.mdpi.com/article/10.3390/chemosensors10120527/s1>, Figure S1: EDS spectra of  $\text{Zr}_{1-x}\text{Eu}_x\text{TiO}_4$  ( $x = 0$ (a), 0.01 (b), 0.05(c)) and the relative content of different elements in the samples derived from EDS analysis. The signals of  $\text{Eu}^{3+}$  was not detected at lower doping concentration ( $x \leq 0.01$ ); The Si signals detected are from the silicon substrate used to support the powdered samples; Figure S2: PL spectra of the  $\text{ZrTiO}_4$  recorded at 77 K and room temperature ( $\lambda_{\text{ex}} = 340$  nm). The luminescence peaking at  $\sim 725$  nm and the band above 800 nm are probably from crystal-field transitions of traces of transition metal impurities (e.g.,  $\text{Cr}^{3+}$ ,  $\text{Mn}^{4+}$ ), which were commonly contained in the commercially available  $\text{TiO}_2$  starting materials; Figure S3: Fluorescence decay trace of 650 nm emission in  $\text{ZrTiO}_4$  upon excitation at 430 nm at 77 K; Figure S4: The luminescence intensity of 612 (a) 520 nm (b) emissions in  $\text{Zr}_{1-x}\text{Eu}_x\text{TiO}_4$  ( $x = 0.0001, 0.0005, 0.002, 0.005, 0.01, 0.05$ ) phosphors upon host excitation at 300 and 340 nm; Figure S5: Fluorescence microscopy image ( $200\times$ ) of  $\text{Zr}_{0.99}\text{Eu}_{0.01}\text{TiO}_4$  under excitation of 340–370 nm; Figure S6: Excitation spectra of  $\text{Zr}_{1-x}\text{Eu}_x\text{TiO}_4$  ( $x = 0, 0.0001, 0.0005, 0.002, 0.005, 0.01, 0.05$ ) phosphors of  $\text{Eu}^{3+}$  emissions ( $\lambda_{\text{em}} = 613$  nm); Figure S7: Fluorescence decay traces of  $^5\text{D}_0$  level  $\text{Eu}^{3+}$  ions in  $\text{Zr}_{1-x}\text{Eu}_x\text{TiO}_4$  ( $x = 0.0001, 0.05$ ) ( $\lambda_{\text{ex}} = 534$  nm  $\lambda_{\text{em}} = 613$  nm) at 300 K and fitting curves; Figure S8: Temperature resolution  $\delta_T$  of  $\text{Zr}_{1-x}\text{Eu}_x\text{TiO}_4$  ( $x = 0.0001$ ) temperature sensing material in the temperature range from 153 K to 313 K; Table S1: The excitation and emission wavelengths used in decay kinetics measurements, lifetime constants and percentage of two compo-



nents, reduced chi-squared value for exponential and biexponential fitting and average lifetimes in different samples ( $Zr_{1-x}Eu_xTiO_4$ ).

**Author Contributions:** Conceptualization, G.-H.P.; Methodology, G.-H.P.; Software, A.G.; Formal analysis, A.G., H.W. (Huajun Wu), L.Z. (Liangliang Zhang), L.Z. (Ligong Zhang) and H.W. (Hao Wu); Investigation, A.G., G.-H.P. and J.Z.; Resources, H.W. (Huajun Wu), L.Z. (Liangliang Zhang), H.W. (Hao Wu) and J.Z.; Data curation, A.G., L.Z. (Ligong Zhang) and H.W. (Hao Wu); Writing—original draft, A.G.; Writing—review & editing, G.-H.P. and J.Z.; Visualization, A.G. and H.W. (Huajun Wu); Supervision, G.-H.P.; Project administration, G.-H.P.; Funding acquisition, G.-H.P. and J.Z. All authors have read and agreed to the published version of the manuscript.

**Funding:** This work was partially supported by National Natural Science Foundation of China (Grant No. 12074374, 12074373, 11874055, 11974346, 11904361, 52072361 and 52102192), Youth Innovation Promotion Association CAS No. 2020222, Key Research and Development Program of Jilin province (20200401050GX, 20200401004GX and 20210201024GX), Changchun science and technology planning project (Grant No. 21ZGY05), the Opening Project Key Laboratory of Transparent Opto-functional Inorganic Material, Chinese Academy of Sciences.

**Conflicts of Interest:** The authors declare no conflict of interest.

## References

1. Diaz, A.L. Progress in understanding host-sensitized excitation processes in luminescent materials. *ECS J. Solid State Sci. Technol.* **2019**, *8*, R14–R26. [[CrossRef](#)]
2. Marciniak, L.; Kniec, K.; Elżbiaciak-Piecka, K.; Trejgis, K.; Stefanska, J.; Dramićanin, M. Luminescence thermometry with transition metal ions. A review. *Coordin. Chem. Rev.* **2022**, *469*, 214671–214702. [[CrossRef](#)]
3. Bednarkiewicz, A.; Drabik, J.; Trejgis, K.; Jaque, D.; Ximendes, E.; Marciniak, L. Luminescence based temperature bio-imaging: Status, challenges, and perspectives. *Appl. Phys. Rev.* **2021**, *8*, 011317–011371. [[CrossRef](#)]
4. Jaque, D.; Vetrone, F. Luminescence nanothermometry. *Nanoscale* **2012**, *4*, 4301–4326. [[CrossRef](#)]
5. Zheng, B.; Fan, J.; Chen, B.; Qin, X.; Wang, J.; Wang, F.; Deng, R.; Liu, X. Rare-earth doping in nanostructured inorganic materials. *Chem. Rev.* **2022**, *122*, 5519–5603. [[CrossRef](#)] [[PubMed](#)]
6. Bianco, A.; Gusmano, G.; Freer, R.; Smith, P. Zirconium titanate microwave dielectrics prepared via polymeric precursor route. *J. Eur. Ceram. Soc.* **1999**, *19*, 959–963. [[CrossRef](#)]
7. Polliotto, V.; Albanese, E.; Livraghi, S.; Indyka, P.; Sojka, Z.; Pacchioni, G.; Giamello, E. Fifty–Fifty Zr–Ti solid solution with a  $TiO_2$ -Type structure: Electronic structure and photochemical properties of zirconium titanate  $ZrTiO_4$ . *J. Phys. Chem. C* **2017**, *121*, 5487–5497. [[CrossRef](#)]
8. Cosentino, I.C.; Muccillo, E.N.S.; Muccillo, R. Development of zirconia-titania porous ceramics for humidity sensors. *Sens. Actuat. B-Chem.* **2003**, *96*, 677–683. [[CrossRef](#)]
9. Park, Y.  $Zr_{0.98}Sn_{0.02}TiO_4$  single crystal in a low electric field: Birefringence, dielectric, and synchrotron X-ray studies. *Phys. Rev. B* **2000**, *62*, 8794–8801. [[CrossRef](#)]
10. Lynch, R.W.; Morosin, B. Thermal expansion, compressibility, and polymorphism in hafnium and zirconium titanates. *J. Am. Ceram. Soc.* **1972**, *55*, 409–413. [[CrossRef](#)]
11. Bordet, P.; Mchale, A.; Santoro, A.; Roth, R. Powder neutron diffraction study of  $ZrTiO_4$ ,  $Zr_5Ti_7O_{24}$ , and  $FeNb_2O_6$ . *J. Solid State Chem.* **1986**, *64*, 30–46. [[CrossRef](#)]
12. Bayer, G.; Hofmann, M.; Gauckler, L.J. Effect of ionic substitution on the thermal expansion of  $ZrTiO_4$ . *J. Am. Ceram. Soc.* **1991**, *74*, 2205–2208. [[CrossRef](#)]
13. Mchale, A.; Roth, R. Investigation of the phase-transition in  $ZrTiO_4$  and  $ZrTiO_4$ - $SnO_2$  solid-solutions. *J. Am. Ceram. Soc.* **1983**, *66*, C18–C20. [[CrossRef](#)]
14. Oanh, L.M.; Do, D.B.; Hung, N.M.; Thang, D.V.; Phuong, D.T.; Ha, D.T.; Van Minh, N. Formation of Crystal structure of zirconium titanate  $ZrTiO_4$  powders prepared by Sol–Gel method. *J. Electron. Mater.* **2016**, *45*, 2553–2558. [[CrossRef](#)]
15. de Lucena, P.R.; Roberto, L.E.; Pontes, F.M.; Longo, E.; Pizani, P.S.; Arana, V.J. Photoluminescence: A probe for short, medium and long-range self-organization order in oxide. *J. Solid State Chem.* **2006**, *179*, 3997–4002. [[CrossRef](#)]
16. Shi, Q.; You, F.; Huang, S.; Cui, J.; Huang, Y.; Tao, Y. Host sensitization of  $Tb^{3+}$  through  $Gd^{3+}$  in  $Na_3Gd(BO_3)_3:Tb^{3+}$ . *J. Alloys Compd.* **2016**, *654*, 441–444. [[CrossRef](#)]
17. Eempicki, A. The physics of inorganic scintillators. *J. Appl. Spectrosc.* **1995**, *62*, 787–802. [[CrossRef](#)]
18. Richard, C.P.; Blasse, G. Energy transfer in concentrated systems. In *Luminescence and Energy Transfer*; Springer: Berlin/Heidelberg, Germany, 1980; Volume 42, pp. 43–96.
19. Blasse, G. Luminescence of inorganic solids: From isolated centres to concentrated systems. *Prog. Solid State Chem.* **1988**, *18*, 79–171. [[CrossRef](#)]
20. Alarcon, J.; Blasse, G. Luminescence of  $Eu^{3+}$ -doped lanthanum titanate ( $La_2TiO_5$ ), a system with one-dimensional energy migration. *J. Phys. Chem. Solids* **1992**, *53*, 677–680. [[CrossRef](#)]

21. Dehaart, L.; Devries, A.; Blasse, G. On the photoluminescence of semiconducting titanates applied in photoelectrochemical cells. *J. Solid State Chem.* **1985**, *59*, 291–300. [[CrossRef](#)]
22. Pan, G.; Zhang, L.; Wu, H.; Qu, X.; Wu, H.; Hao, Z.; Zhang, L.; Zhang, X.; Zhang, J. On the luminescence of  $\text{Ti}^{4+}$  and  $\text{Eu}^{3+}$  in monoclinic  $\text{ZrO}_2$ : High performance optical thermometry derived from energy transfer. *J. Mater. Chem. C* **2020**, *8*, 4518–4533. [[CrossRef](#)]
23. Yu, D.; Li, H.; Zhang, D.; Zhang, Q.; Meijerink, A.; Suta, M. One ion to catch them all: Targeted high-precision Boltzmann thermometry over a wide temperature range with  $\text{Gd}^{3+}$ . *Light-Sci. Appl.* **2021**, *10*, 236–247. [[CrossRef](#)] [[PubMed](#)]
24. Liao, C.; Chen, F.; Wu, H.; Wu, H.; Zhang, L.; Pan, G.; Liu, F.; Wang, X.; Zhang, J. Afterglow-intensity-ratio-based temperature sensing using a persistent phosphor. *J. Mater. Chem. C* **2022**, *10*, 11884–11890. [[CrossRef](#)]
25. Marciniak, L.; Bednarkiewicz, A.; Streck, W. Tuning of the up-conversion emission and sensitivity of luminescent thermometer in  $\text{LiLaP}_4\text{O}_{12}$ : Tm, Yb nanocrystals via  $\text{Eu}^{3+}$  dopants. *J. Lumin.* **2017**, *184*, 179–184. [[CrossRef](#)]
26. Yu, H.; Su, W.; Chen, L.; Deng, D.; Xu, S. Excellent temperature sensing characteristics of europium ions self-reduction  $\text{Sr}_3\text{P}_4\text{O}_{13}$  phosphors for ratiometric luminescence thermometer. *J. Alloys Compd.* **2019**, *806*, 833–840. [[CrossRef](#)]
27. Maciejewska, K.; Pozniak, B.P.; Tikhomirov, M.; Kobylin'ska, A.; Marciniak, L. Synthesis, cytotoxicity assessment and optical properties characterization of colloidal  $\text{GdPO}_4$ :  $\text{Mn}^{2+}$ ,  $\text{Eu}^{3+}$  for high sensitivity luminescent nanothermometers operating in the physiological temperature range. *Nanomaterials* **2020**, *10*, 421. [[CrossRef](#)]
28. Kniec, K.; Marciniak, L. Spectroscopic properties of  $\text{LaGaO}_3$ : V,  $\text{Nd}^{3+}$  nanocrystals as a potential luminescent thermometer. *Phys. Chem. Chem. Phys.* **2018**, *20*, 21598–21606. [[CrossRef](#)]
29. Kolesnikov, I.E.; Mamonova, D.V.; Kurochkin, M.A.; Kolesnikov, E.Y.; Lähderanta, E. Multimode luminescence thermometry based on emission and excitation spectra. *J. Lumin.* **2021**, *231*, 117828–117831. [[CrossRef](#)]
30. Elzbiaciak, K.; Bednarkiewicz, A.; Marciniak, L. Temperature sensitivity modulation through crystal field engineering in  $\text{Ga}^{3+}$  co-doped  $\text{Gd}_3\text{Al}_{5-x}\text{Ga}_x\text{O}_{12}$ :  $\text{Cr}^{3+}$ ,  $\text{Nd}^{3+}$  nanothermometers. *Sens. Actuat. B-Chem.* **2018**, *269*, 96–102. [[CrossRef](#)]
31. Mykhaylyk, V.; Kraus, H.; Zhydachevskyy, Y.; Tsiumra, V.; Luchechko, A.; Wagner, A.; Suchocki, A. Multimodal non-contact luminescence thermometry with Cr-doped oxides. *Sensors* **2020**, *20*, 5259. [[CrossRef](#)]
32. Marciniak, L.; Bednarkiewicz, A.; Kowalska, D.; Streck, W. A new generation of highly sensitive luminescent thermometers operating in the optical window of biological tissues. *J. Mater. Chem. C* **2016**, *4*, 5559–5563. [[CrossRef](#)]
33. Katsumata, T.; Nakayama, A.; Kano, Y.; Aizawa, H.; Komuro, S. IEEE Characteristics of Ti-doped sapphire for fluorescence thermo-sensor. In Proceedings of the 2007 International Conference on Control, Automation and Systems, Seoul, Republic of Korea, 17–20 October 2007; pp. 1025–1028.
34. Drabik, J.; Cichy, B.; Marciniak, L. New type of nanocrystalline luminescent thermometers based on  $\text{Ti}^{3+}/\text{Ti}^{4+}$  and  $\text{Ti}^{4+}/\text{Ln}^{3+}$  ( $\text{Ln}^{3+} = \text{Nd}^{3+}$ ,  $\text{Eu}^{3+}$ ,  $\text{Dy}^{3+}$ ) luminescence intensity ratio. *J. Phys. Chem. C* **2018**, *122*, 14928–14936. [[CrossRef](#)]
35. Wang, C.; Jin, Y.; Yuan, L.; Wu, H.; Ju, G.; Li, Z.; Liu, D.; Lv, Y.; Chen, L.; Hu, Y. A spatial/temporal dual-mode optical thermometry platform based on synergetic luminescence of  $\text{Ti}^{4+}$ - $\text{Eu}^{3+}$  embedded flexible 3D micro-rod arrays: High-sensitive temperature sensing and multi-dimensional high-level secure anti-counterfeiting. *Chem. Eng. J.* **2019**, *374*, 992–1004. [[CrossRef](#)]
36. Dramićanin, M.D. Sensing temperature via downshifting emissions of lanthanide-doped metal oxides and salts. A review. *Methods Appl. Fluoresc.* **2016**, *4*, 042001–042024. [[CrossRef](#)] [[PubMed](#)]
37. Michael, N.G.; Per-Anders, H.; Helmer, F.; Ola, N. Luminescent properties of europium titanium phosphate thin films deposited by atomic layer deposition. *RSC Adv.* **2017**, *7*, 8051–8059. [[CrossRef](#)]
38. Veronica, P.; Marco, B.; Rosanna, R.; Asmaa El, K.; Manuela, R.; Giancarlo, D.V.; Francesco, C. Characterization and Luminescence of  $\text{Eu}^{3+}$ - and  $\text{Gd}^{3+}$ -Doped Hydroxyapatite  $\text{Ca}_{10}(\text{PO}_4)_6(\text{OH})_2$ . *Crystals* **2020**, *10*, 806. [[CrossRef](#)]
39. de Haart, L.G.J.; Boessenkoo, H.J.; Blasse, G. Photoelectrochemical properties of titanium niobate ( $\text{TiNb}_2\text{O}_7$ ) and titanium tantalate ( $\text{TiTa}_2\text{O}_7$ ). *Mater. Chem. Phys.* **1985**, *13*, 85–90. [[CrossRef](#)]
40. Blasse, G.; Bril, A. The influence of crystal structure on the fluorescence of oxidic niobates and related compounds. *Z. Phys. Chem.* **1968**, *57*, 187–202. [[CrossRef](#)]
41. Blasse, G. Optical electron-transfer between metal-ions and its consequences. *Struct. Bond.* **1991**, *76*, 153–187.
42. Haynes, W.M.; Bruno, T.J.; David, R. *CRC Handbook of Chemistry and Physics*, 96th ed.; CRC Press: Boca Raton, FL, USA, 2015.
43. Krebs, M.A.; Condrate, R.A. A Raman spectral characterization of various crystalline mixtures in the  $\text{ZrO}_2$ - $\text{TiO}_2$  and  $\text{HfO}_2$ - $\text{TiO}_2$  systems. *J. Mater. Sci. Lett.* **1988**, *7*, 1327–1330. [[CrossRef](#)]
44. Nowak, M.; Kauch, B.; Szperlich, P. Determination of energy band gap of nanocrystalline SbSI using diffuse reflectance spectroscopy. *Rev. Sci. Instrum.* **2009**, *80*, 046107–046110. [[CrossRef](#)] [[PubMed](#)]
45. Chang, D.; Lin, P.; Tseng, T. Optical properties of  $\text{ZrTiO}_4$  films grown by radio-frequency magnetron sputtering. *J. Appl. Phys.* **1995**, *77*, 4445–4451. [[CrossRef](#)]
46. Toyozawa, Y. Electrons, Holes and Excitons in Deformable Lattice. In *Relaxation of Elementary Excitations*; Ryogo, K., Eiichi, H., Eds.; Springer: Berlin/Heidelberg, Germany, 1980; pp. 3–18.
47. Blasse, G. The influence of crystal structure on the luminescence of tantalates and niobates. *J. Solid State Chem.* **1988**, *72*, 72–79. [[CrossRef](#)]
48. Blasse, G.; Bril, A. On the  $\text{Eu}^{3+}$  Fluorescence in mixed metal oxides. III. Energy transfer in  $\text{Eu}^{3+}$ -activated tungstates and molybdates of the type  $\text{Ln}_2\text{WO}_6$  and  $\text{Ln}_2\text{MoO}_6$ . *J. Chem. Phys.* **1966**, *45*, 2350–2355. [[CrossRef](#)]

49. Blasse, G.; Bril, A. Fluorescence of  $\text{Eu}^{3+}$ -activated sodium lanthanide titanates ( $\text{NaLn}_{1-x}\text{Eu}_x\text{TiO}_4$ ). *J. Chem. Phys.* **1968**, *48*, 3652–3656. [[CrossRef](#)]
50. Ran, W.; Noh, H.; Park, S.; Lee, B.; Kim, J.; Jeong, J.; Shi, J.  $\text{Er}^{3+}$ -activated  $\text{NaLaMgWO}_6$  double perovskite phosphors and their bifunctional application in solid-state lighting and non-contact optical thermometry. *Dalton Trans.* **2019**, *48*, 4405–4412. [[CrossRef](#)]
51. Shi, R.; Lin, L.; Dorenbos, P.; Liang, H. Development of a potential optical thermometric material through photoluminescence of  $\text{Pr}^{3+}$  in  $\text{La}_2\text{MgTiO}_6$ . *J. Mater. Chem. C* **2017**, *5*, 10737–10745. [[CrossRef](#)]
52. Glais, E.; Pellerin, M.; Castaing, V.; Alloyeau, D.; Touati, N.; Viana, B.; Chaneac, C. Luminescence properties of  $\text{ZnGa}_2\text{O}_4:\text{Cr}^{3+}$ ,  $\text{Bi}^{3+}$  nanophosphors for thermometry applications. *RSC Adv.* **2018**, *8*, 41767–41774. [[CrossRef](#)]
53. Zhu, Y.; Li, C.; Deng, D.; Yu, H.; Li, H.; Wang, L.; Shen, C.; Jing, X.; Xu, S. High-sensitivity based on  $\text{Eu}^{2+}/\text{Cr}^{3+}$  co-doped  $\text{BaAl}_{12}\text{O}_{19}$  phosphors for dual-mode optical thermometry. *J. Lumin.* **2021**, *237*, 118142–118150. [[CrossRef](#)]
54. Li, L.; Tong, Y.; Chen, J.; Chen, Y.; Ghulam, A.A.; Chen, L.; Pang, T.; Guo, H. Up-conversion and temperature sensing properties of  $\text{Na}_2\text{GdMg}_2(\text{VO}_4)_3:\text{Yb}^{3+}, \text{Er}^{3+}$  phosphors. *J. Am. Ceram. Soc.* **2021**, *105*, 384–391. [[CrossRef](#)]
55. Piotrowski, W.M.; Ristic, Z.; Dramićanin, M.D.; Marciniak, Ł. Modification of the thermometric performance of the lifetime-based luminescent thermometer exploiting  $\text{Ti}^{3+}$  emission in  $\text{SrTiO}_3$  and  $\text{CaTiO}_3$  by doping with lanthanide ions. *J. Alloys Compd.* **2022**, *906*, 164398–164406. [[CrossRef](#)]